

# seg2med: a segmentation-based medical image generation framework using denoising diffusion probabilistic models

Zeyu Yang, Zhilin Chen, Yipeng Sun, Anika Strittmatter, Anish Raj, Ahmad Allababidi, Johann S. Rink, and Frank G. Zöllner, *Senior Member, IEEE*

**Abstract**—In this study, we present seg2med, an advanced medical image synthesis framework that uses Denoising Diffusion Probabilistic Models (DDPM) to generate high-quality synthetic medical images with the conditional anatomical masks from TotalSegmentator. The framework successfully synthesizes CT and MR images from segmentation masks derived from real patient data and XCAT digital phantoms, achieving a Structural Similarity Index Measure (SSIM) of  $0.94 \pm 0.02$  for CT and  $0.89 \pm 0.04$  for MR images compared to ground-truth images of real patients, and a Feature Similarity Index Measure (FSIM) of  $0.78 \pm 0.04$  for CT images from XCAT. The framework demonstrates its generative capability with a Fréchet Inception Distance (FID) of 3.62 for CT image generation. Furthermore, seg2med demonstrates the capability to generate paired multimodal CT and MR images with consistent anatomical structures and performs image conversion between CT and MR modalities, achieving a SSIM of  $0.91 \pm 0.03$  for the conversion of MR to CT and  $0.77 \pm 0.04$  for the conversion of CT to MR. Despite the challenges associated with incomplete anatomical information in segmentation masks, the framework achieves promising results, highlighting its potential in cross-modality synthesis and multimodal imaging applications.

The framework also excels at generating high anatomical fidelity CT images, achieving a mean Dice coefficient of  $> 0.90$  for 11 abdominal organs and  $> 0.80$  for 34 organs from the 59 organs in 58 test cases, with the highest Dice achieved for the scapula right of  $0.96 \pm 0.01$ . Using the TotalSegmentator toolkit, seg2med enhances its versatility by enabling segmentation mask generation for diverse datasets. This supports applications such as clinical imaging, data augmentation, multimodal image synthesis, and the development of diagnostic algorithms.

**Index Terms**—computed tomography, medical image generation, deep learning.

## I. INTRODUCTION

COMPUTED tomography (CT) and magnetic resonance imaging (MRI) are two important modalities in medical

Z. Yang, Z. Chen, A. Strittmatter, A. Raj, and F. G. Zöllner are with the Computer Assisted Clinical Medicine, Medical Faculty Mannheim, Heidelberg University, Mannheim, Germany, e-mail: zeyu.yang@medma.uni-heidelberg.de, anika.strittmatter@medma.uni-heidelberg.de, anish.raj@medma.uni-heidelberg.de, frank.zoellner@medma.uni-heidelberg.de.

Y. Sun is with the Pattern Recognition Lab, Friedrich-Alexander-University Erlangen-Nuremberg, Erlangen, Germany.

A. Allababidi and J. Rink are with the Department of Radiology and Nuclear Medicine, University Medical Center Mannheim, Mannheim, Germany, e-mail: johann.rink@umm.de

Z. Yang, Z. Chen, A. Strittmatter, A. Raj, and F. G. Zöllner are with the Mannheim Institute for Intelligent Systems in Medicine, Medical Faculty Mannheim, Heidelberg University, Mannheim, Germany

imaging. MRI is particularly effective for visualizing soft tissue structures with high contrast, while CT offers complementary insights with precise visualization of bone anatomy and essential electron density information for accurate dosimetric calculations in radiotherapy.

Due to their unique strengths, combining CT and MRI in multimodal imaging has become routine in clinical practice [1]. This integration enhances diagnostic precision in abdominal and pelvic imaging, improving assessment accuracy across a range of conditions. For example, in total hip arthroplasty (THA) patients, CT accurately measures lesion size in osteolysis assessments, while MRI is better suited for detecting small lesions in challenging locations. Together, they provide a complete assessment, balancing MRI's sensitivity with CT's volumetric precision [2]. Similarly, in liver cancer imaging, CT serves as an initial tool to survey metastases, while MRI with liver-specific contrast agents offers additional diagnostic clarity for small or indeterminate lesions. This combination supports comprehensive characterization and staging, especially for patients with chronic liver disease or those preparing for surgery, as CT provides anatomical details and MRI enhances soft tissue contrast [3].

Despite their complementary roles in medical imaging, the lack of paired CT and MRI data remains a significant challenge, as these scans are typically performed independently, leading to increased costs, nonrigid misalignment issues, and limited availability of high-quality, matched datasets for advancing medical imaging research. To address these challenges, medical image synthesis has emerged as a promising solution [4], [5]. This technique establishes a mapping function to transform a known source image into a desired target image, effectively enabling cross-modality image synthesis and addressing data scarcity by generating realistic synthetic images [6]. Recent advances in generative neural networks have led to algorithms that produce realistic high-quality medical images, supporting applications in noise reduction, artifact removal, segmentation, and registration [7], [8]. One common synthesis task is image conversion, typically translating between various medical imaging modalities. Kalantar et al. developed a framework with UNet, UNet++, and CycleGAN to generate pelvic T1-weighted MRI from CT images. Their CycleGAN model produces high-quality MRI without requiring spatial alignment, improving segmentation, and MRI-only planning for pelvic radiotherapy [9]. Similarly, Simkó et al. developed a robust synthetic CT (sCT) gen-

eration framework using quantitative maps (proton density, T1, and T2) to enhance generalization across MRI contrasts and scanners. This approach outperformed contrast-specific models and demonstrated effectiveness in radiotherapy planning with varied MRI contrasts [10]. Baldini et al. compared the pix2pix [11] and BrainClustering for synthesizing T2-weighted images from T1-weighted inputs, finding that the pix2pix with ResNet achieved the highest accuracy. These synthetic images strengthen segmentation models, particularly in scenarios where specific MRI sequences are missing [12].

However, these approaches rely on paired multimodal data, which is difficult to obtain, motivating alternative approaches. For instance, Bauer et al. employed a CycleGAN model to generate multimodal synthetic CT and MR images from XCAT phantoms [13], supporting multimodal registration algorithms [14]. While GANs, like those used in these studies, generate high-resolution images, they often struggle with training stability and consistency [9], [11], [12], [14]. To address these limitations, Denoising Diffusion Probabilistic Models (DDPMs) have emerged, offering stable training and enhanced anatomical detail preservation by progressively denoising images.

Building on these strengths, Han et al. introduced MedGen3D, a DDPM-based framework that generates paired 3D images and segmentation masks for thoracic CT and brain MRI, achieving spatial consistency and anatomical accuracy within single modalities [15]. Similarly, Dorjsembe et al. presented Med-DDPM, a diffusion model generating high-resolution brain MRIs from segmentation masks, with applications in data anonymization and brain tumor segmentation [16].

These studies highlight the importance of effective guidance in generative training but reveal key limitations. Most focus on single-modality synthesis, limiting their use in multimodal contexts essential for comprehensive diagnostics. Additionally, reliance on existing datasets can constrain image quality if training data lacks diversity, and current methods still struggle with aligning images across modalities, especially for non-rigid anatomy.

Recently, TotalSegmentator has emerged as a powerful tool for segmenting CT and MRI images, capable of identifying various anatomical structures, including organs, bones, muscles, and vessels. It achieves high accuracy, with a Dice similarity coefficient of 0.943 for CT and 0.824 for MRI, and it adapts to diverse clinical settings while requiring minimal computational resources [17], [18]. Its applications include organ volumetry, disease characterization, radiation therapy planning, and large-scale radiological studies, making it an ideal choice for advancing medical image segmentation workflows. Notably, TotalSegmentator can address the data diversity issue in medical image synthesis by generating unlimited, high-quality anatomical masks from various CT and MR scans. These masks can serve as inputs for synthetic image generation, mitigating the reliance on scarce paired datasets and enabling more robust and generalizable synthesis models. Thus, this study selected TotalSegmentator as the primary segmentation tool for processing real CT and MR images used in this research.

Building on the concept of segmentation-guided medical image synthesis, this study presents a framework based on DDPMs. The approach incorporates a preprocessing pipeline that uses TotalSegmentator to generate segmented organ masks, resolves overlapping areas with adjustments, and simulates CT or MRI images for training inputs. The framework evaluates 2-channel DDPMs for multimodal image generation compared to established models such as UNet, CycleGAN, and pix2pix. Comprehensive analyses of the generated images include quantitative metrics, modality conversion efficacy, and their impact on segmentation performance, offering insights into the potential of DDPMs in medical imaging.

## II. METHODS AND MATERIALS

### A. Framework

The framework is depicted in Figure 1.

In the Data Preprocessing stage, the TotalSegmentator toolkit is utilized to generate organ segmentation masks from CT and MR images. These masks serve as the foundation for creating paired input data for training. Overlapping regions are resolved using adjustments to ensure accurate representation of anatomical structures. Next, CT Hounsfield Unit (HU) and MR sequence values are allocated to the segmentations, generating CT and MR masks that simulate realistic imaging characteristics. The processed masks are then paired with corresponding CT or MR images, forming the dataset for training the synthesis model.

The Image Synthesis stage employs DDPMs to generate synthetic CT and MR images. The forward diffusion process introduces noise to the input masks, creating progressively noisy versions of the images. The reverse denoising process, guided by a denoising U-Net, reconstructs high-quality synthetic images from these noisy inputs. Separate DDPMs are trained for CT and MR image synthesis to optimize the performance for each modality.

Finally, in the Evaluation stage, the generated images are assessed through comprehensive quantitative and qualitative analyses. Evaluation include segmentation accuracy evaluation and image quality evaluation. The performance of the framework is validated by comparing the synthetic images against ground-truth data, ensuring the effectiveness of the proposed method in multimodal medical imaging tasks.

### B. Networks

We investigated a conditional denoising diffusion probabilistic model (cDDPM) [19] in this study. It features a diffusion-model-UNet designed with a channel sequence of (64, 128, 256, 256). At each level, two residual blocks were incorporated, and the final layer was enhanced with an attention layer with eight attention heads, each with 32 channels. To address the specific task of image synthesis, the source mask image was appended to the noisy image as an extra channel. Consequently, this modification resulted in a 2-channel input configuration for the UNet component within the diffusion model.

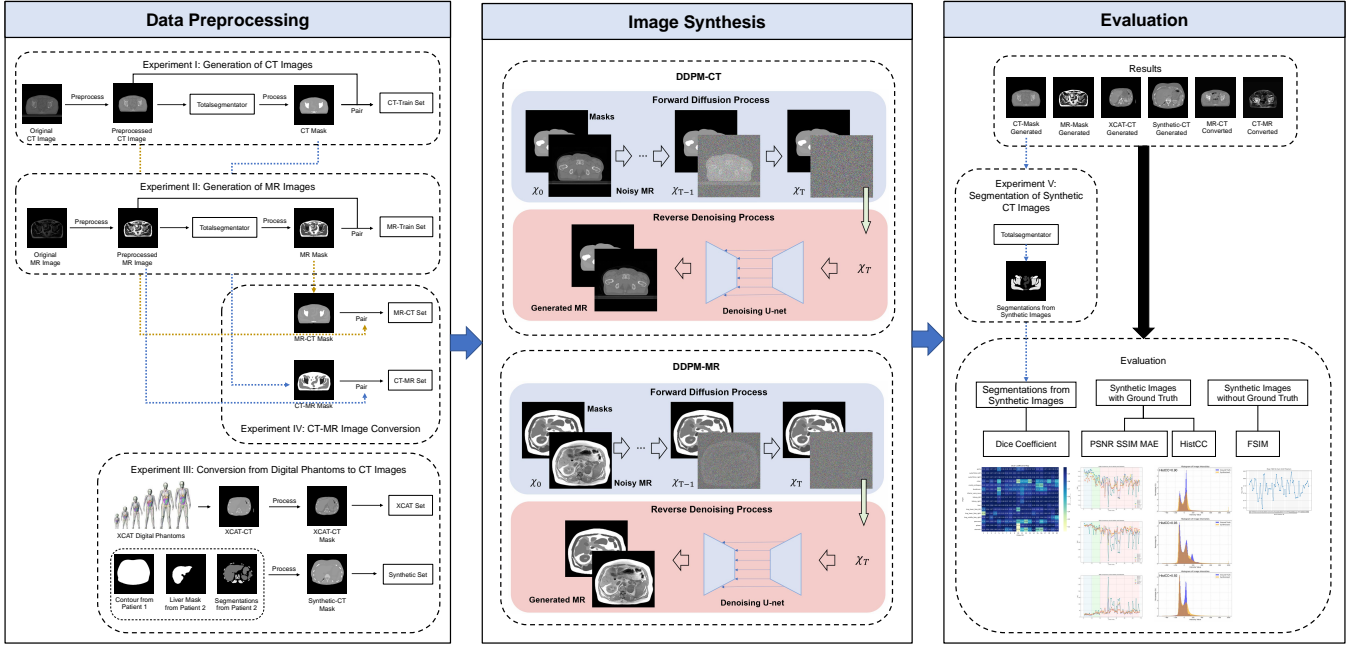


**Fig. 1.** Illustration for the seg2med framework. The process begins with data preprocessing, including the generation of CT and MR masks. The second stage, image synthesis, employs diffusion probabilistic models (DDPM-CT and DDPM-MR) to generate synthetic MR and CT images. Finally, the evaluation phase assesses the synthetic images using segmentation performance and image quality metrics (e.g., Dice coefficient, PSNR, SSIM, MAE, HistCC, and FSIM). The framework highlights the importance of combining ground-truth-based and non-ground-truth-based evaluations for comprehensive analysis.

The performance of this 2-channel DDPM on CT image generation (DDPM-CT) was compared with other three supervised generative models: a UNet incorporating attention blocks [20], a pix2pix [11] and a CycleGAN [21]. The UNet, pix2pix, and CycleGAN were trained using their standard settings.

### C. Datasets

In this study, several datasets from different studies were used to add the generalizability of this framework.

The first dataset is the pelvis dataset of task 1 from SynthRAD2023 challenge with a total of 180 patients with paired MR and CT images in the training dataset, and a total of 30 patients with MR images in the validation dataset [22]. The MR images are acquired with a T1 weighted gradient echo sequence. For details on the dataset please refer to [22].

For CT images of 180 patients, the data are divided into 170 training samples and 10 test samples. For MR images of 180 patients, this splitting continues to be used: the images of the same 170 patients are used for training and the rest 10 patients with the 30 patients in the SynthRAD-validation dataset, totally 40 patients, are used for testing.

The second dataset is an internal abdomen-CT dataset (named Internal Abdominal CT) with 163 patients, including 78 patients presenting with aortic dissection(AD) with abdominal extent between 2010/01/01 and 2021/03/01 and 85 patients of AD-negative cases. For details on the data set please refer to [23]. This dataset was split into a training set of 153 patients and a test set of 10 patients.

The third dataset consists of abdominal CT and T1-weighted MRI of the liver. These were acquired on 39 patients as part

of the M2OLIE project. This dataset contains 48 CT images and 91 MR T1-weighted Volumetric Interpolated Breath-hold Examination (VIBE) sequence images (in-phase and opposed-phase) in transversal orientation. These images were registered by our previously developed convolutional neural network. For details on the data set please refer to [24]. All the CT images were used for testing. The MRI data of 34 patients (81 image volumes) were used for training and the MRI data of 5 patients (10 image volumes) were used for test. This dataset is referred to as M2OLIE Abdominal CT/MTI in the following.

The fourth dataset was from the Extended Cardiac-Torso (XCAT) phantom data [13]. The Library of XCAT anatomy files provides an additional 56 adult models (33 males and 23 females) of varying heights (from 153 cm to 186.4 cm) and weights (from 52 kg to 120 kg) at different ages (from 18 to 78). For these models, we generate one abdomen CT-XCAT volume and one abdomen MR-XCAT volume for each XCAT model. For CT-XCAT volume, the simulated CT value preset in the XCAT2 software is used [13]. For MR-XCAT volume, the signal equation of the VIBE sequence is used to recalculate the MR signal value so that each slice in volumes has an image intensity value similar to that of the MR image measured by the real VIBE sequence. Since the XCAT-generated masks do not have corresponding Ground Truth images, the XCAT dataset was only used for testing our approach.

For the CT framework, by pooling the data, 323 CT image volumes were used for training and 59 CT image volumes for testing. For the MR framework, 251 MR image volumes were used for training and 20 MR image volumes were used for testing. For both frameworks, 56 XCAT phantoms were used

for testing only. An overview of the implemented datasets is presented in Table I.

#### D. Image Pre-processing

The image pre-processing step involved image normalization, contour regularization, mask generation, and the assignment of simulated grayscale values.

The primary goal of CT image pre-processing was to remove outlier pixels and normalize the images. First, the CT images were windowed using a level of 0 and a width of 2000 to retain lung tissue structures and main bone structures. Subsequently, the images were normalized to a range of [0, 1]. The resolution was resampled to  $1.0 \times 1.0 \text{ mm}^2$  in X-Y plane since this study focused on 2D image generation. For the Z-direction, the resolution was reversed during the stacking of 2D slices to form a 3D volume for each patient, to ensure that the generated slices could be stacked into a volume corresponding to each patient. After windowing and normalization, body contours were extracted from the images to remove irrelevant parts such as arms and the scanner bed, further standardizing the spatial range of the images. The extracted contour map was used not only to regulate the target image but also to ensure consistency in the spatial areas of the generated mask images. Mask generation was a critical step in pre-processing the source images, involving segmentation, value reassignment, and contour regularization. The TotalSegmentator toolkit was employed to generate segmentations of up to 117 anatomical structures from the CT images. Each anatomical class in the segmentation mask was then assigned with an appropriate HU value to create simulated CT masks.

For MR images, pre-processing aimed to normalize intensity values and create accurate segmentation masks. The 10th percentile (p10) and 90th percentile (p90) of intensity values were calculated for each MR volume to define the windowing range. The image intensity values were restricted within this range and then normalized. Similar to the CT images, body contours were extracted and applied to ensure spatial consistency. The TotalSegmentator toolkit was also used for generating MRI segmentation masks. Contour regularization was applied to remove arm regions and ensure alignment with the spatial range of the target images. Next, the VIBE sequence was used to reassign signal intensity values to various organs and tissues within the segmentation map. This step ensured that the simulated MR masks reflected the specific characteristics of the MRI sequence. Consequently, a simulated MR image was generated for each patient.

#### E. Experiments

Overall, we have conducted five experiments: the generation of CT images, the generation of MR images, the conversion from digital phantoms to CT images including XCAT-to-CT conversion and synthetic-to-CT conversion, bi-directional image conversion between CT and MR modalities, and segmentation evaluation of synthetic CT images.

1) *Experiment I:* First, the four models were trained using 170 pelvis CT images from the SynthRAD training set (SynthRAD Pelvis) [22] and 153 abdomen CT images from the

internal dataset (Internal Abdomen CT) [23] for 200 epochs. During training, the input images consisted of CT image masks with reassigned HU values for organ segmentations. The target images were the corresponding ground truth CT images. After training, they were evaluated and compared on 10 CT images of unseen patients from the SynthRAD Pelvis, 10 CT images of unseen patients from Internal Abdomen, and all patients from the M2OLIE Abdomen dataset. The synthetic CT images were assessed by comparison with the ground truth, and the performance of the four implemented models was evaluated specifically in the context of CT image generation. For training the 2-channel DDPM, an initial learning rate of 0.0002, Adam optimizer with  $\beta_1 = 0.9$  and  $\beta_2 = 0.999$ , and Mean Squared Error (MSE) loss was used.

2) *Experiment II:* The 2-channel DDPM-MR models were trained using 170 pelvis MR images from the SynthRAD training set (SynthRAD Pelvis) [22] and 81 abdomen MR T1-weighted images from the M2OLIE project (M2OLIE Abdomen) [7]. During early-phase experiments, we observed that the segmentations produced by the *total mr* task of the TotalSegmentator toolkit were insufficient for synthesizing high-quality MR images. This limitation arose because subcutaneous fat, torso fat, and skeletal muscle are critical for maintaining image fidelity in MR imaging. To address this, we combined the segmentation maps from *total mr* and *tissue types mr* tasks into a comprehensive organ map. The merged segmentation maps were then regularized using body contours and assigned MR sequence values generated through the sequence formula. Subsequently, the MR masks were utilized as training inputs, with the corresponding ground truth MR images serving as the target outputs. The training process was conducted over 300 epochs to achieve convergence. Due to differences in acquisition sequences between the two datasets, they were used separately for training and testing. The models were then evaluated on 40 MR images of unseen patient from the SynthRAD Pelvis and 10 MR images of unseen patients from M2OLIE Abdomen.

3) *Experiment III:* The trained DDPM-CT model was employed to generate CT images using masks from digital phantoms that lacked corresponding ground truth images. CT image generation was performed for 56 Extended Cardiac-Torso (XCAT) digital phantoms [13]. Additionally, a composite digital phantom, created by merging segmentations and body contour of multiple patients, was used to generate a CT image within our framework, showcasing the model's robustness and its potential for data augmentation.

4) *Experiment IV:* The image conversion between CT and MR modalities was performed by inputting CT masks into the DDPM-MR model and MR masks into the DDPM-CT model. 10 paired pelvis CT and images from the SynthRAD dataset were utilized in this experiment. Due to differences in organ class indices between CT and MR segmentations in the TotalSegmentator toolkit, segmentations from the source modality were first converted to match the segmentation scheme of the target modality. These converted segmentations were then regularized using the body contour derived from the source image and assigned simulated values corresponding to the target modality. The resulting images were subsequently

**TABLE I.** Overview of Implemented Datasets

Dataset	Anatomy	Total	CT		MR		Test
			Train	Test	Train	Test	
SynthRAD CT/MR	Pelvis	180	170	10	210	170	40
Internal Abdomen CT	Abdomen	163	153	10	0	0	0
M2OLIE Abdomen CT/MR	Abdomen	48	0	48	91	81	10
XCAT	Abdomen	56	0	56	56	0	56

evaluated against the paired images of the target modality.

5) *Experiment V*: The synthetic abdomen CT images generated from segmentations of 10 patients from the internal dataset (Internal Abdomen) and 48 patients from the M2OLIE Abdomen CT/MR dataset were further segmented using the TotalSegmentator toolkit and evaluated by comparing with the original input segmentations.

#### F. Evaluation Metrics

In Experiment I, II and IV, the synthetic CT and MR images (sCT and sMR) were evaluated against the original CT and MR images using several image quality assessment metrics, including SSIM, Mean Absolute Error (MAE), Peak Signal-to-Noise Ratio (PSNR). SSIM evaluates the structural similarity between the generated image and the ground truth image, taking into account factors like luminance, contrast, and structure. SSIM values range from -1 to 1, with 1 indicating a perfect similarity. MAE measures the average absolute difference between the generated image and the ground truth image. A lower MAE indicates that the generated image is closer to the ground truth image in terms of pixel-level differences. PSNR (Peak Signal-to-Noise Ratio) measures the ratio between the maximum possible power of a signal (the pixel values of the original image) and the power of the noise (the difference between the original and generated image). A higher PSNR value is generally associated with better image quality. Additionally, the consistency between the histograms of synthetic images and ground truth images was evaluated using Histogram Correlation Coefficient (HistCC).

To determine the statistical significance of the improvements in the SSIM, MAE, and PSNR, we performed statistical hypothesis tests. We compared the DDPM with each other model and applied a Mann-Whitney U test as the metrics are non-normally distributed. Our null hypothesis states that the DDPM did not lead to improvements in either metric. The null hypothesis is rejected if  $p < 0.05$ .

The Frèchet Inception Distance (FID) [25] is a widely used metric for evaluating image synthesis, quantifying the similarity between two distributions—typically real and generated images. Lower FID scores indicate greater similarity, with values approaching zero reflecting better performance. In this study, we employed the standard implementation using the Inception-V3 model [26] to compute the FID between the synthesized images and the ground-truth images. Since the synthesized medical images are single-channel and have a broader pixel value range compared to RGB images, we adapted them by duplicating to three channels and normalizing the pixel values to the range of 0–1. A P-test is not required

for FID, as it inherently quantifies the differences between the distributions of real and generated images.

Feature Similarity Index (FSIM) is suitable for evaluating synthetic CT images generated from XCAT-derived masks in experiment III, as it does not rely on ground truth for comparison. It is a feature-based metric, evaluates the perceptual similarity of images by focusing on critical low-level features such as edges and textures, making it especially effective for assessing structural detail [27].

The Dice coefficient was used to quantify the overlap between segmented regions in synthetic and target images in experiment V, offering insight into organ-level accuracy.

## III. RESULTS

### A. Experiment I: Generation of CT Images

Table II provides the quantitative results for CT image generation achieved by each implemented model. The models were trained using the training datasets from the SynthRAD Pelvis and the Internal Abdomen, while the M2OLIE Abdomen consisted of “unseen” patients for evaluation. The results indicate that, although DDPM shows no significant advantage over other models in validation on the SynthRAD Pelvis and the Internal Abdomen, it demonstrates a clear improvement for the M2OLIE Abdomen. Specifically, DDPM achieves the highest SSIM of  $0.93 \pm 0.02$ , the lowest MAE of  $40.05 \pm 13.15$ , a relatively high PSNR of  $26.16 \pm 1.62$ , and the lowest standard deviation across all metrics, indicating its superior and more stable performance compared to other models. Overall, DDPM achieves the highest SSIM of  $0.94 \pm 0.02$ , the lowest MAE of  $36.79 \pm 24.34$ , the lowest FID of 3.62, although the highest PSNR is observed with UNet ( $28.05 \pm 4.12$ ).

Table III presents the results of the significance tests, demonstrating that DDPM significantly outperformed other models in SSIM and MAE metrics ( $p < 0.05$ ) but performed significantly worse than other models in terms of PSNR ( $p < 0.05$ ).

Representative examples of three CT image slices from a patient in each dataset are illustrated in Figure 2, with SSIM noted on each synthetic CT image. These examples highlight DDPM’s ability to achieve strong quantitative metrics while preserving anatomical details such as the aorta, kidney, and pancreas, as evident in the field of view (FOV) boxes.

An analysis of the histograms comparing synthetic CT images from each model with the ground-truth CT images of the same patients shows that the DDPM-generated images closely match the real CT images in terms of intensity distribution, as illustrated in Figure 3. For the example patient, the histogram correlation coefficients (HistCCs) of the DDPM-generated images from all three datasets exceed 0.90.

**TABLE II.** Quantitative evaluation of the four models on the three test CT datasets. The SynthRAD Pelvis includes ten unseen patients from the synthrad dataset [22]. The Internal Abdomen includes ten unseen patients from an internal abdomen-CT dataset [23]. The M2OLIE Abdomen is an abdomen CT dataset from the M2OLIE project, which is not included in training and is an independent dataset [24]. Values are presented as mean $\pm$ standard deviation. Better results are indicated by higher SSIM and PSNR values, along with lower MAE and FID values.

(a) SSIM				
mean $\pm$ std	UNet	CycleGAN	pix2pix	DDPM
SynthRAD Pelvis	0.96 $\pm$ 0.02	0.96 $\pm$ 0.01	0.96 $\pm$ 0.01	0.96 $\pm$ 0.01
Internal Abdomen	0.95 $\pm$ 0.03	0.94 $\pm$ 0.02	0.94 $\pm$ 0.02	0.95 $\pm$ 0.02
M2OLIE Abdomen	0.89 $\pm$ 0.06	0.92 $\pm$ 0.03	0.92 $\pm$ 0.03	0.93 $\pm$ 0.02
overall	0.92 $\pm$ 0.05	0.93 $\pm$ 0.04	0.93 $\pm$ 0.04	0.94 $\pm$ 0.02
(b) PSNR				
mean $\pm$ std	UNet	CycleGAN	pix2pix	DDPM
SynthRAD Pelvis	32.36 $\pm$ 1.79	31.39 $\pm$ 1.45	32.00 $\pm$ 2.28	30.00 $\pm$ 2.60
Internal Abdomen	29.29 $\pm$ 3.13	28.28 $\pm$ 2.66	28.82 $\pm$ 2.72	28.00 $\pm$ 2.51
M2OLIE Abdomen	25.98 $\pm$ 3.88	26.37 $\pm$ 3.10	26.49 $\pm$ 3.03	26.16 $\pm$ 1.62
overall	28.05 $\pm$ 4.12	27.90 $\pm$ 3.71	27.97 $\pm$ 3.62	27.58 $\pm$ 3.48
(c) MAE				
mean $\pm$ std	UNet	CycleGAN	pix2pix	DDPM
SynthRAD Pelvis	21.35 $\pm$ 5.08	17.36 $\pm$ 2.25	15.98 $\pm$ 3.11	19.60 $\pm$ 4.94
Internal Abdomen	31.33 $\pm$ 12.82	29.10 $\pm$ 9.92	26.61 $\pm$ 9.32	28.95 $\pm$ 10.16
M2OLIE Abdomen	61.56 $\pm$ 45.49	42.26 $\pm$ 21.53	40.69 $\pm$ 20.89	40.05 $\pm$ 13.15
overall	45.30 $\pm$ 37.44	39.70 $\pm$ 30.16	37.22 $\pm$ 27.05	36.79 $\pm$ 24.34
(d) FID				
	UNet	CycleGAN	pix2pix	DDPM
SynthRAD Pelvis	8.56	7.62	3.48	4.46
Internal Abdomen	12.78	10.60	6.74	5.30
M2OLIE Abdomen	15.35	14.34	10.14	5.01
overall	11.26	9.98	6.25	3.62

**TABLE III.** P-values from the Mann-Whitney U test ( $p<0.05$ ) assessing the significance of differences in SSIM, PSNR, and MAE metrics between DDPM and other models

Model	SSIM	PSNR	MAE
DDPM vs. UNet	<0.00001	<0.00001	<0.00001
DDPM vs. CycleGAN	<0.00001	<0.00001	0.00710
DDPM vs. pix2pix	<0.00001	<0.00001	<0.00001

To provide a comprehensive comparison of the four models, Figure 4 presents line charts and box plots of the metrics for synthetic CT images of test patients across all three datasets. In line charts, the x-axis represents the patient index, and the y-axis indicates the mean metric value for the generated CT images of each patient. The three datasets are distinguished by background colors. In the box plots, the x-axis represents the four models, and the y-axis shows the metric values. Additionally, the exact values for all evaluated patients are displayed as points, with each dataset distinguished by a unique point color. The line charts and box plots show that DDPM consistently delivers stable and excellent performance across all datasets, while the other models exhibit poorer performance for some patients, particularly in the new dataset (e.g., patients 41, 42, and 43). This observation is further supported by DDPM's lowest standard deviation across all metrics in Table II.

**TABLE IV.** Metrics for assessing quality of synthetic MR images

	SSIM	PSNR	MAE	FID
SynthRAD Pelvis	0.89 $\pm$ 0.04	20.56 $\pm$ 3.52	9.70 $\pm$ 4.68	4.64
M2OLIE Abdomen	0.56 $\pm$ 0.07	22.67 $\pm$ 6.05	17.75 $\pm$ 1.68	36.66

#### B. Experiment II: Generation of MR Images

Two MR datasets were utilized for the second experiment: the pelvis MR image dataset from Task 1 of the SynthRad2023 dataset (SynthRAD Pelvis) and the M2OLIE abdomen MR dataset (M2OLIE Abdomen). The test results were summarized in Table IV, with the value range of the generated MR images normalized to [0, 255]. The pelvis MR images generated by our framework achieved a mean SSIM close to 0.90, demonstrating high image quality. In contrast, the generated abdomen MR images for M2OLIE Abdomen exhibited lower quality, with a mean SSIM of 0.56  $\pm$  0.07. This disparity is attributed to the larger dataset size and superior image quality of the SynthRAD Pelvis compared to the M2OLIE Abdomen. As shown in Figure 5, the synthesized pelvis MR images generated by DDPM display well-preserved image details, particularly in skeletal and muscle tissue.

#### C. Experiment III: Conversion from Digital Phantoms to CT Images

Table V presents the mean FSIM values for synthesized CT images generated from 56 XCAT digital phantoms and a digital phantom created by merging segmentations and body contours from multiple patients. The CT images generated from segmentations of real patient images in Experiment I achieved a relatively high mean FSIM of 0.82 $\pm$ 0.08, while the CT images synthesized from XCAT digital phantoms exhibited a comparable FSIM of 0.78  $\pm$  0.04, indicating a high degree of structural consistency with real images. In contrast, the CT image generated from the merged-segmentation digital phantom showed a lower FSIM of 0.45  $\pm$  0.02. Figure 6 illustrates a qualitative assessment of synthetic CT images generated by DDPM for XCAT and synthetic digital phantoms. Three image slices are selected from different XCAT models (Model89, Model106, Model140), while the bottom three slices are derived from a single synthetic digital phantom created by merging segmentations from three different patients. As shown in the figure, the synthetic CT images generated from XCAT phantoms preserve realistic anatomical structures, whereas the image synthesized from the synthetic digital phantom does not. This qualitative observation aligns with the FSIM values displayed on the upleft side of the figures. Figure 7 provides an overview of the FSIM values for the CT images synthesized from the 56 XCAT digital phantoms. Most phantoms achieved FSIM values above 0.75, reflecting high-quality image synthesis with well-preserved structural details. The observed variation in FSIM values may be attributed to differences in anatomical complexity and feature representation among the phantoms.

#### D. Experiment IV: CT-MR Image Conversion

The dataset comprising 10 paired pelvis CT and MR images was utilized in this experiment. Table VI summarizes the mean

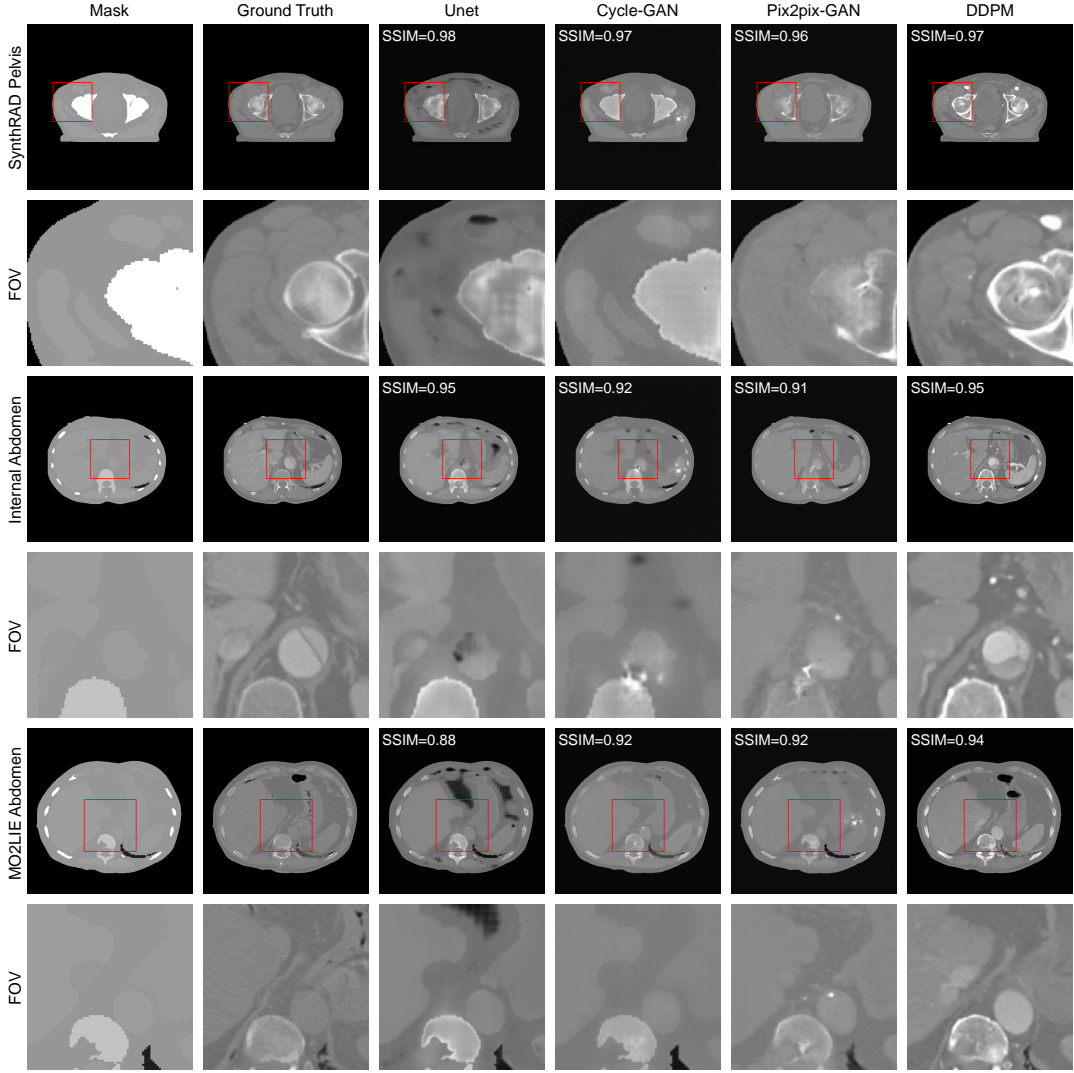


**Fig. 2.** Qualitative comparison of synthetic CT images generated by four models across the three datasets. This figure presents one representative image slice per dataset, illustrating the outputs of the four models: UNet, CycleGAN, pix2pix-GAN, and DDPM. The first column displays the input mask, followed by the ground truth image. Subsequent columns show synthetic images generated by each model. Key metrics (SSIM, PSNR, and MAE) are provided for quantitative comparison. Focused fields of view (FOVs) within the red boxes highlight regions of interest to enhance visual comparison of structural details and model performance.

**TABLE V.** FSIM for assessing quality of synthetic images from XCAT digital phantoms and synthetic digital phantoms created by segmentations from multiple patients

	Synthetic CT (Experiment I)	XCAT CT	Synthetic Patient CT
FSIM	$0.82 \pm 0.08$	$0.78 \pm 0.04$	$0.45 \pm 0.02$

SSIM, PSNR, and MAE values for the 10 converted CT and MR images. The results indicate that the converted CT images achieve a high SSIM of  $0.91 \pm 0.03$ , demonstrating their high structural fidelity. In contrast, the converted MR images exhibit lower quality, with a relatively low SSIM of  $0.77 \pm 0.04$  and a PSNR of  $15.53 \pm 2.02$ . Figure 8 displays the converted images alongside the ground truth images of the target modality and the synthesized images from Experiment I and Experiment II for the same patient. Examples from two patients are included

**TABLE VI.** Metrics for assessing quality of image conversion between CT and MR images.

	SSIM	PSNR	MAE
MR-to-CT	$0.91 \pm 0.03$	$22.76 \pm 2.35$	$47.14 \pm 30.38$
CT-to-MR	$0.77 \pm 0.04$	$15.53 \pm 1.47$	$16.32 \pm 4.66$

in the figure. The comparison shows that the converted CT images effectively preserve critical anatomical structures, while the converted MR images maintain good quality and similarity to ground truth but lack detail in certain tissues.

#### E. Experiment V: Segmentation Evaluation of Synthetic CT Images

The synthetic abdomen CT images generated from the segmentations of 10 patients from the internal dataset (Internal Abdomen) and 48 patients from the M2OLIE Abdomen

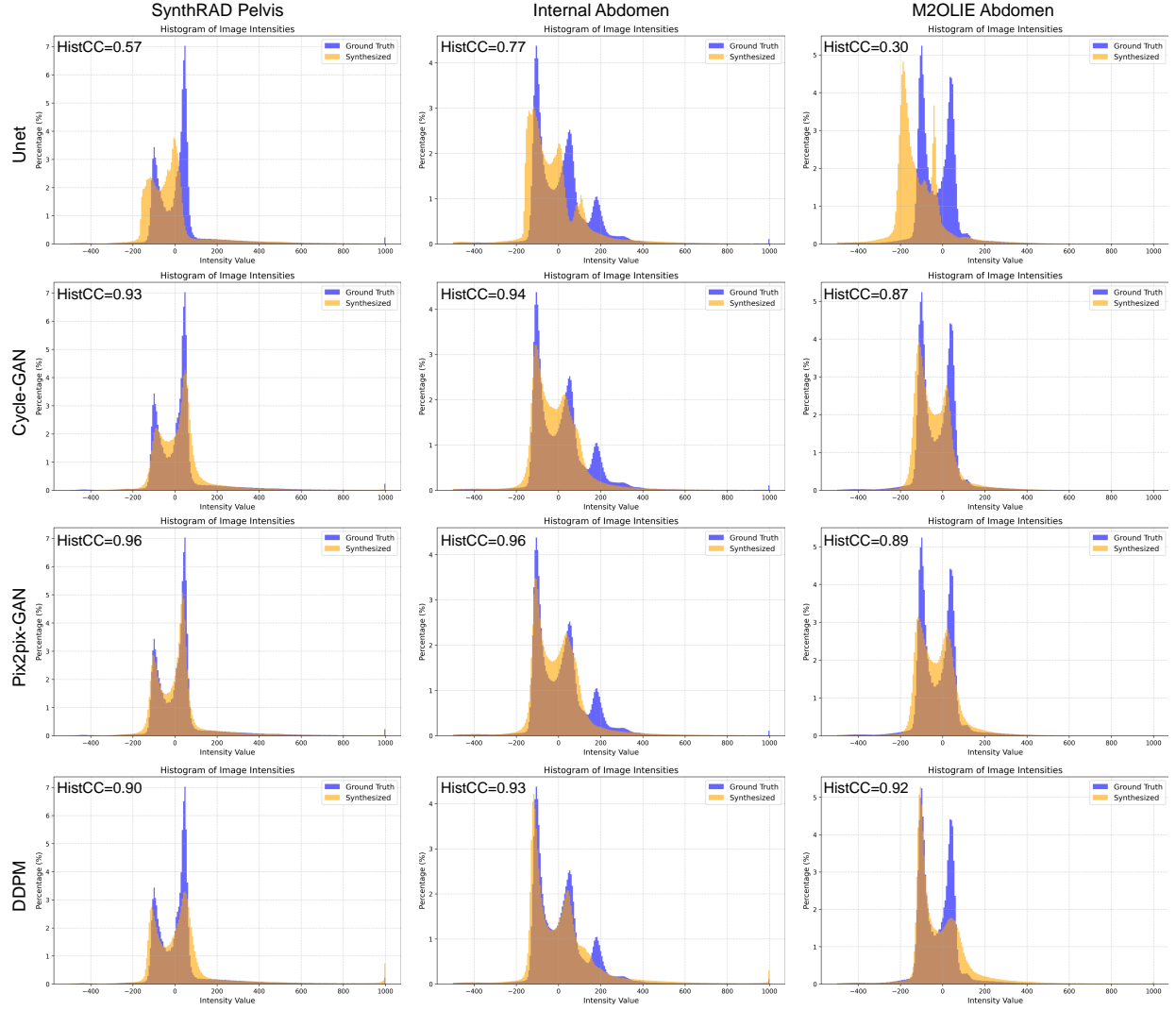


**Fig. 3.** Comparison of image intensities distribution across models and datasets. Histograms of image intensities for ground truth (blue) and synthesized (orange) images corresponding to the image slices are shown. Histograms are provided for three datasets and four deep learning models: UNet, CycleGAN, pix2pix, and DDPM. The Histogram Correlation Coefficient (HistCC) values, representing the similarity between the intensity distributions of synthesized and ground truth images, are calculated and displayed for each case. These visualizations highlight the alignment of intensity distributions achieved by each model within the respective datasets.

dataset (M2OLIE Abdomen) were further segmented using the Totalsegmentator toolkit’s *total* task. The mean Dice coefficients between the segmentations of each abdominal organ from the synthetic and ground truth images of these 58 patients are presented in Table VII. The results indicate that 11 of the 59 organs achieved a mean Dice coefficient greater than 0.90, demonstrating high consistency with the original CT segmentations. These organs include Autochthon Left, Autochthon Right, Kidney Left, Kidney Right, Liver, Rib Left 11, Scapula Right, Spinal Cord, Vertebrae L3, Vertebrae T10, and Vertebrae T11. Additionally, 34 of the 59 organs achieved a mean Dice coefficient exceeding 0.80.

Figure 9 provides the organ segmentation results for six different organs across six patient cases, with the corresponding Dice scores annotated on each image. The figure illustrates that the segmentations of autochthon (left and right), kidney, and liver consistently achieve high Dice coefficients above 0.90 for

all six patients. The segmentation of the colon in one patient also exceeds 0.90, while the segmentations of the spleen and stomach exceed 0.90 in four of the six cases.

Figure 10 depicts a heatmap of Dice coefficients for 16 organ segmentations across 20 patients, covering a total of 320 cases. Higher values (darker blue) represent better segmentation overlap between synthetic image segmentations and ground truth segmentations. The heatmap reveals that 223 out of the 320 cases (69.69%) achieved a Dice coefficient greater than 0.90, highlighting the strong agreement between synthetic and ground truth segmentations for most cases.

#### IV. DISCUSSION

In this study, we proposed seg2med, an image generation framework including segmentation, image processing, image synthesis using DDPM, and evaluation steps. The framework demonstrated its capability to generate high-quality CT and

**TABLE VII.** Mean Dice coefficients for different organs

Organ	Dice	Organ	Dice	Organ	Dice
Adrenal Gland Left	0.82±0.08	Lung Upper Lobe Left	0.68±0.23	Vertebrae L1	0.74±0.31
Adrenal Gland Right	0.76±0.27	Lung Upper Lobe Right	0.69±0.25	Vertebrae L2	0.80±0.18
Aorta	0.87±0.19	Pancreas	0.73±0.22	Vertebrae L3	0.91±0.00
Autochthon Left	0.92±0.13	Portal Vein and splenic vein	0.63±0.21	Vertebrae L4	0.72±0.02
Autochthon Right	0.93±0.06	Rib Left 5	0.74±0.17	Vertebrae T6	0.69±0.00
Colon	0.69±0.25	Rib Left 6	0.85±0.10	Vertebrae T7	0.58±0.36
Costal Cartilages	0.79±0.15	Rib Left 7	0.84±0.13	Vertebrae T8	0.74±0.18
Duodenum	0.74±0.19	Rib Left 8	0.86±0.10	Vertebrae T9	0.88±0.07
Esophagus	0.77±0.26	Rib Left 9	0.84±0.11	Vertebrae T10	0.92±0.05
Gallbladder	0.31±0.20	Rib Left 10	0.86±0.13	Vertebrae T11	0.91±0.03
Heart	0.86±0.17	Rib Left 11	0.90±0.06	Vertebrae T12	0.89±0.14
Iliopsoas Left	0.83±0.16	Rib Left 12	0.88±0.02	Pulmonary Vein	0.81±0.00
Iliopsoas Right	0.61±0.29	Rib Right 5	0.71±0.18	Spinal Cord	0.94±0.04
Inferior Vena Cava	0.87±0.12	Rib Right 6	0.74±0.25	Spleen	0.85±0.22
Kidney Left	0.93±0.12	Rib Right 7	0.83±0.14	Sternum	0.72±0.25
Kidney Right	0.93±0.11	Rib Right 8	0.86±0.12	Stomach	0.77±0.23
Liver	0.93±0.13	Rib Right 9	0.81±0.12	Small Bowel	0.66±0.26
Lung Lower Lobe Left	0.82±0.20	Rib Right 10	0.76±0.20	Scapula Left	0.85±0.00
Lung Lower Lobe Right	0.82±0.21	Rib Right 11	0.66±0.34	Scapula Right	0.96±0.01
Lung Middle Lobe Right	0.88±0.13	Rib Right 12	0.76±0.28		

MR images based on segmentations from real patient data and digital phantoms. Across all datasets, the framework achieved an SSIM of  $> 0.90$  for CT images from real segmentations, an SSIM of  $> 0.80$  for MR images from real segmentations, and an FSIM of  $> 0.70$  for CT images from XCAT phantoms. The framework further demonstrates its generative capability with a Fréchet Inception Distance (FID) of 3.62 for CT image generation. It also achieves a SSIM of  $> 0.90$  for MR-to-CT images and a SSIM of  $> 0.70$  for CT-to-MR images. These results indicate that the framework generalizes well to both real-world and digital phantom data, supporting its potential to accelerate dataset creation for the development of clinical algorithms. Furthermore, utilizing the Totalsegmentator toolkit enhances the framework's ability to process diverse datasets and generate segmentation masks for medical image synthesis, making it highly versatile.

#### A. Comparison to Published Medical Image Synthesis Methods

The proposed framework outperformed established generative models such as UNet, CycleGAN, and pix2pix in synthesizing pelvic and abdominal CT images (Figure 2). Specifically, the 2-channel DDPM maintained superior structural integrity and realistic presentation of organs such as the liver, spleen, and aorta as shown in the FOVs. The quantitative results in Table II show that the DDPM achieved the highest SSIM of  $0.94 \pm 0.02$  and the lowest MAE of  $36.79 \pm 24.34$ , demonstrating its alignment with real images. However, its relatively lower PSNR of  $27.58 \pm 3.48$  suggests room for further improvement in the denoising process.

This framework represents a novel application of AI-based auto-segmentation tools, specifically the TotalSegmentator toolkit, to generate full-organ masks for medical image synthesis. This approach differentiates itself from other recent methods that employ simpler or less detailed segmentation masks. For instance, Dorjsembe et al. Med-DDPM showcased the application of diffusion models for 3D semantic brain MRI synthesis. Using segmentation masks, their approach

generated anatomically coherent and visually realistic images, achieving a Dice score of 0.6207 in tumor segmentation tasks, which is close to the real image Dice score of 0.6531. Similarly, Xing et al. proposed an Unsupervised Mask (UM)-guided synthesis strategy. Their method used limited manual segmentation labels to condition GAN-based synthesis, producing high-quality synthetic images that realistically captured human anatomy and pathological variations. Their framework demonstrated significant improvements in fidelity, diversity, and utility through the innovative use of unsupervised masks. Compared to these studies, seg2med uniquely focuses on generating multimodal medical images, including paired CT and MR scans. It shows a significant capability to produce high-quality synthetic CT and MR images, achieving a SSIM of  $0.94 \pm 0.02$  for CT and  $0.89 \pm 0.04$  for MR images compared to ground truth data. This highlights the accuracy of the model and its effectiveness in maintaining structural and textural fidelity. By using detailed, AI-generated full-organ masks, it ensures structural consistency across modalities and enhances the utility of synthesized images for both research and clinical applications.

A notable strength of this framework is its ability to generate paired CT and MR images from the same anatomical structure. Using segmentations from the same patient, the framework ensures anatomical consistency across modalities. It achieves a high SSIM of  $0.91 \pm 0.03$  for MR-to-CT images and  $0.77 \pm 0.04$  for CT-to-MR images, with both demonstrating good quality and similarity to ground truth, though CT-to-MR images exhibit a lack of detail in some areas. This feature is particularly advantageous for applications that require multimodal imaging, such as image registration, fusion, or training deep learning models that depend on consistent cross-modality datasets. It also provides a valuable tool for developing diagnostic algorithms that rely on complementary information from both CT and MR images.

It also demonstrates significant potential for synthesizing medical images using digital phantoms, specifically with XCAT models. This capability positions this method as a

robust tool for generating synthetic data across diverse scenarios, including those with limited availability of real-world datasets. In comparison to Bauer et al.’s study, which utilized a CycleGAN to extend small datasets and achieved SSIM values of  $0.94 \pm 0.02$  for CT and  $0.59 \pm 0.04$  for MR images, this framework offers several advantages. First, it employs larger datasets, which enhances its ability to generalize and produce high-quality synthetic images. Second, it has been proven stable even when applied to completely unseen datasets, demonstrating its robustness and adaptability. These features underline the superiority of this approach in synthesizing multimodal medical images, paving the way for broader applications in clinical algorithm development and research requiring extensive and varied datasets.

Multimodal medical image conversion is an increasingly mature field that offers promising solutions to the challenge of insufficient paired medical images. This approach is particularly valuable for applications such as noise reduction, artifact removal, image segmentation, and registration. In this study, we utilized a paired pelvis CT and MR dataset from Task 1 of the SynthRAD2023 challenge. The best metrics from SynthRAD2023 were achieved by SMU-MedVision, developed by Zhou et al., which employed a state-of-the-art 2.5D UNet++ with a ResNet101 backbone. Their framework reported an SSIM of  $0.885 \pm 0.029$ , a PSNR of  $29.61 \pm 1.79$ , and an MAE of  $58.83 \pm 13.41$  in the validation phase [28]. Comparatively, our framework achieved higher metrics, with an SSIM of  $0.91 \pm 0.03$ , a PSNR of  $22.76 \pm 2.35$ , and an MAE of  $47.14 \pm 30.38$ . Although our framework outperformed SMU-MedVision in these metrics, we cannot definitively conclude its superiority for several reasons. First, our framework used 10 patients from the training set of Task 1 for paired image synthesis since the ground truth CT images were not provided within the validation set by the challenge. The difference in data distribution between the training and validation sets of SynthRAD2023 may have significantly influenced model performance. Second, our framework utilized more datasets for training, which enhanced its image-generation capabilities. Despite these concerns, the results clearly demonstrate the potential of our framework for translating MR images to CT images by converting MR masks to CT masks.

Our framework also demonstrated robust performance in generating CT images with high anatomical consistency compared to the original CT images. By analyzing the segmentations derived from synthetic images against those from ground truth images, we observed that, among 58 test abdomen CT images, 11 out of 59 abdominal organs achieved a mean Dice coefficient exceeding 0.90, while 34 organs surpassed a mean Dice coefficient of 0.80, with the scapula right has the highest mean Dice coefficient of  $0.96 \pm 0.01$ . This high level of consistency underscores the framework’s ability to accurately replicate anatomical structures, suggesting its potential for applications requiring precise anatomical fidelity, such as image segmentation, diagnostic algorithm training, and multimodal imaging studies.

### B. Limitations

Despite its strengths, this framework has limitations. The reliance on 2D image generation is a limitation, as it results in non-smooth cross-sectional reconstructions in lateral and coronal planes, reducing the continuity between slices. Additionally, the sampling process is relatively slow, requiring approximately 30 seconds per  $512 \times 512$  slice with 500 timesteps on an NVIDIA RTX A6000 GPU. Attempts to implement 3D-DDPM were constrained by GPU memory, allowing generation only for  $128 \times 128 \times 128$  volumes. Future work should focus on optimizing 3D generation to achieve a balance between inference speed and image quality. Furthermore, the framework lacks conditional generation capabilities, limiting its ability to synthesize images with pathological features. For instance, although the internal abdomen CT dataset includes 78 aortic dissection patients, identifying pathological features necessitates continuous 3D volumes, which was not supported by the current framework. Future efforts will aim to train the 3D-seg2med network with disease-specific conditions and evaluate synthetic pathological features through collaborations with clinicians and diagnostic AI tools. Lastly, the quantitative results for CT images converted from MR images were relatively poor, with a mean SSIM of  $0.77 \pm 0.04$ , a PSNR of  $15.53 \pm 1.47$ , and an MAE of  $16.32 \pm 4.66$ . This performance discrepancy can be attributed to the lower generalizability of the DDPM-MR model, due to its training on a smaller dataset compared to the DDPM-CT model. To address this limitation, future work will focus on incorporating a larger and more diverse MR dataset to enhance the model’s robustness and performance. Additionally, further optimization of the training process and exploration of advanced techniques for handling limited data scenarios will be prioritized.

## V. CONCLUSION

In this study, we introduced seg2med, an innovative image generation framework that combines segmentation, image processing, image synthesis using Denoising Diffusion Probabilistic Models (DDPM), and evaluation steps. Our framework effectively generates high-quality synthetic CT and MR images from segmentation masks derived from real patient data and XCAT digital phantoms. It achieves SSIM values exceeding 0.90 for CT images and 0.80 for MR images, along with FSIM values above 0.70 for digital phantom CT images. Additionally, with an overall FID score below 4.00 for CT image generation, the framework demonstrates strong generalizability and fidelity across diverse datasets. Furthermore, it successfully generated paired multimodal CT and MR images with consistent anatomical structures, highlighting its potential for multimodal imaging applications.

The framework also showcased its capability to synthesize CT images with high anatomical consistency, achieving a mean Dice coefficient above 0.90 for 11 abdominal organs and above 0.80 for 34 organs across 59 organs of 58 test abdomen CT images. This emphasizes its utility for tasks requiring precise anatomical detail, such as segmentation and clinical algorithm development. Additionally, the integration of the TotalSegmentator toolkit enhanced the framework’s

versatility, allowing it to process diverse datasets and generate segmentation masks for realistic medical image synthesis.

Despite its advancements, the framework requires future work to address limitations such as optimizing 3D generation, incorporating pathological conditions.

Overall, this study highlights the potential of seg2med as a robust and versatile tool for medical image synthesis, offering promising applications in clinical imaging, data augmentation, and the development of advanced diagnostic and therapeutic algorithms. By addressing its current limitations, seg2med could play a pivotal role in shaping the future of medical imaging and AI-driven healthcare solutions.

#### ACKNOWLEDGMENT

This research project is part of the Research Campus M2OLIE and funded by the German Federal Ministry of Education and Research (BMBF) within the Framework "Forschungscampus: public-private partnership for Innovations" under the funding code 13GW0388A and 13GW0747A.

#### REFERENCES

- [1] Q. Lyu and G. Wang, "Conversion between ct and mri images using diffusion and score-matching models," no. arXiv:2209.12104, 2022.
- [2] T. A. Walde, A. Allababidi, D. E. Weiland, S. B. Leung, N. Kitamura, C. J. Sychterz, C. A. J. Engh, H. G. Potter, and C. A. Engh, "Comparison of ct, mri, and radiographs in assessing pelvic osteoanalysis: A cadaveric study," *Clinical Orthopaedics and Related Research*, pp. 138–144, 2005.
- [3] M. R. Oliva and S. Saini, "Liver cancer imaging: role of ct, mri, us and pet," *Cancer Imaging*, pp. 42–46, 2004.
- [4] S. Gómez, D. Mantilla, G. Garzón, E. Rangel, A. Ortiz, F. Sierra-Jerez, and F. Martínez, "APIS: A paired CT-MRI dataset for ischemic stroke segmentation challenge," *Scientific Reports*, vol. 14, no. 1, p. 20543, Sep. 2024.
- [5] S. Dekeyzer, O. Nikoubashman, B. Lutin, J. De Groote, E. Vancaester, S. De Blauwe, D. Hemelsoet, M. Wiesmann, and L. Defreyne, "Distinction between contrast staining and hemorrhage after endovascular stroke treatment: One CT is not enough," *Journal of NeuroInterventional Surgery*, vol. 9, no. 4, pp. 394–398, Apr. 2017.
- [6] V. Kearney, B. P. Ziemer, A. Perry, T. Wang, J. W. Chan, L. Ma, O. Morin, S. S. Yom, and T. D. Solberg, "Attention-Aware Discrimination for MR-to-CT Image Translation Using Cycle-Consistent Generative Adversarial Networks," *Radiol: Artif Intell*, vol. 2, no. 2, p. e190027, Mar. 2020.
- [7] A. Strittmatter, L. R. Schad, and F. G. Zöllner, "Deep learning-based affine medical image registration for multimodal minimal-invasive image-guided interventions – A comparative study on generalizability," *Z Med Phys*, vol. 23, Jun. 2023.
- [8] A. Raj, F. Tollens, L. Hansen, A.-K. Golla, L. R. Schad, D. Nörenberg, and F. G. Zöllner, "Deep Learning-Based Total Kidney Volume Segmentation in Autosomal Dominant Polycystic Kidney Disease Using Attention, Cosine Loss, and Sharpness Aware Minimization," *Diagnostics*, vol. 12, no. 5, p. 1159, May 2022.
- [9] R. Kalantar, C. Messiou, J. M. Winfield, A. Renn, A. Latifoltojar, K. Downey, A. Sohaib, S. Lalondrelle, D.-M. Koh, and M. D. Blackledge, "CT-Based Pelvic T1-Weighted MR Image Synthesis Using UNet, UNet++ and Cycle-Consistent Generative Adversarial Network (CycleGAN)," *Frontiers in Oncology*, vol. 11, p. 665807, Jul. 2021.
- [10] A. Simkó, M. Bylund, G. Jönsson, T. Löfstedt, A. Garpebring, T. Nyholm, and J. Jonsson, "Towards MR contrast independent synthetic CT generation," *Zeitschrift für Medizinische Physik*, vol. 34, no. 2, pp. 270–277, May 2024.
- [11] P. Isola, J. Zhu, T. Zhou, and A. A. Efros, "Image-to-image translation with conditional adversarial networks," in *2017 IEEE Conf on Computer Vision and Pattern Recognition (CVPR)*. Los Alamitos, CA, USA: IEEE Computer Society, Jul 2017, pp. 5967–5976.
- [12] G. Baldini, M. Schmidt, C. Zäske, and L. L. Caldeira, "MRI Scan Synthesis Methods based on Clustering and Pix2Pix," May 2024.
- [13] W. P. Segars, G. Sturgeon, S. Mendonca, J. Grimes, and B. M. W. Tsui, "4D XCAT phantom for multimodality imaging research," *Medical Physics*, vol. 37, no. 9, pp. 4902–4915, Sep. 2010.
- [14] D. F. Bauer, T. Russ, B. I. Waldkirch, C. Tönnes, W. P. Segars, L. R. Schad, F. G. Zöllner, and A.-K. Golla, "Generation of annotated multimodal ground truth datasets for abdominal medical image registration," vol. 16, no. 8, Aug. 2021, pp. 1277–1285.
- [15] K. Han, Y. Xiong, C. You, P. Khosravi, S. Sun, X. Yan, J. Duncan, and X. Xie, "MedGen3D: A Deep Generative Framework for Paired 3D Image and Mask Generation," Jul. 2023.
- [16] Z. Dorjsembe, H.-K. Pao, S. Odonchimed, and F. Xiao, "Conditional Diffusion Models for Semantic 3D Brain MRI Synthesis," *IEEE Journal of Biomedical and Health Informatics*, vol. 28, no. 7, pp. 4084–4093, Jul. 2024.
- [17] J. Wasserthal, H.-C. Breit, M. T. Meyer, M. Pradella, D. Hinck, A. W. Sauter, T. Heye, D. T. Boll, J. Cyriac, S. Yang, M. Bach, and M. Segeroth, "TotalSegmentator: Robust Segmentation of 104 Anatomic Structures in CT Images," *Radiology: Artificial Intelligence*, vol. 5, no. 5, p. e230024, Sep. 2023.
- [18] J. Wasserthal and T. Akinci D'Antonoli, "TotalSegmentator MRI dataset: 298 MRI images with segmentations for 56 anatomical regions," May 2024.
- [19] J. Ho, A. Jain, and P. Abbeel, "Denoising diffusion probabilistic models," in *Proceedings of the 34th International Conference on Neural Information Processing Systems*, ser. NIPS'20. Red Hook, NY, USA: Curran Associates Inc., 2020.
- [20] O. Oktay, J. Schlemper, L. L. Folgoc, M. Lee, M. Heinrich, K. Misawa, K. Mori, S. McDonagh, N. Y. Hammerla, B. Kainz, B. Glocker, and D. Rueckert, "Attention u-net: Learning where to look for the pancreas," in *Medical Imaging with Deep Learning (MIDL)*, B. van Ginneken and M. Welling, Eds., vol. 1, 2018.
- [21] J.-Y. Zhu, T. Park, P. Isola, and A. A. Efros, "Unpaired Image-to-Image Translation using Cycle-Consistent Adversarial Networks," Aug. 2020.
- [22] A. Thummerer, E. van der Bijl, A. Galapon, J. J. C. Verhoeff, J. A. Langendijk, S. Both, C. N. A. T. van den Berg, and M. Maspero, "SynthRAD2023 grand challenge dataset: Generating synthetic CT for radiotherapy," vol. 50, no. 7. Wiley, Jun. 2023, pp. 4664–4674.
- [23] A. Raj, A. Allababidi, H. Kayed, A. L. Gerken, J. Müller, S. O. Schönberg, J. S. Rink, and F. G. Zöllner, "Streamlining acute abdominal aortic dissection management—an ai-based ct imaging workflow," *Journal of Imaging Informatics in Medicine*, pp. 2933–2948, 2024.
- [24] A. Strittmatter and F. G. Zöllner, "Multistep networks for deformable multimodal medical image registration," *IEEE Access*, vol. 12, pp. 82 676–82 692, 2024.
- [25] M. Heusel, H. Ramsauer, T. Unterthiner, B. Nessler, and S. Hochreiter, "GANs Trained by a Two Time-Scale Update Rule Converge to a Local Nash Equilibrium," no. arXiv:1706.08500. arXiv, Jan. 2018.
- [26] C. Szegedy, V. Vanhoucke, S. Ioffe, J. Shlens, and Z. Wojna, "Rethinking the Inception Architecture for Computer Vision," Dec. 2015.
- [27] Lin Zhang, Lei Zhang, Xuanqin Mou, and D. Zhang, "FSIM: A Feature Similarity Index for Image Quality Assessment," *IEEE Transactions on Image Processing*, vol. 20, no. 8, pp. 2378–2386, Aug. 2011.
- [28] E. M. C. Huijben, M. L. Terpstra, A. J. Galapon, *et al.*, "Generating Synthetic Computed Tomography for Radiotherapy: SynthRAD2023 Challenge Report," Jun. 2024.

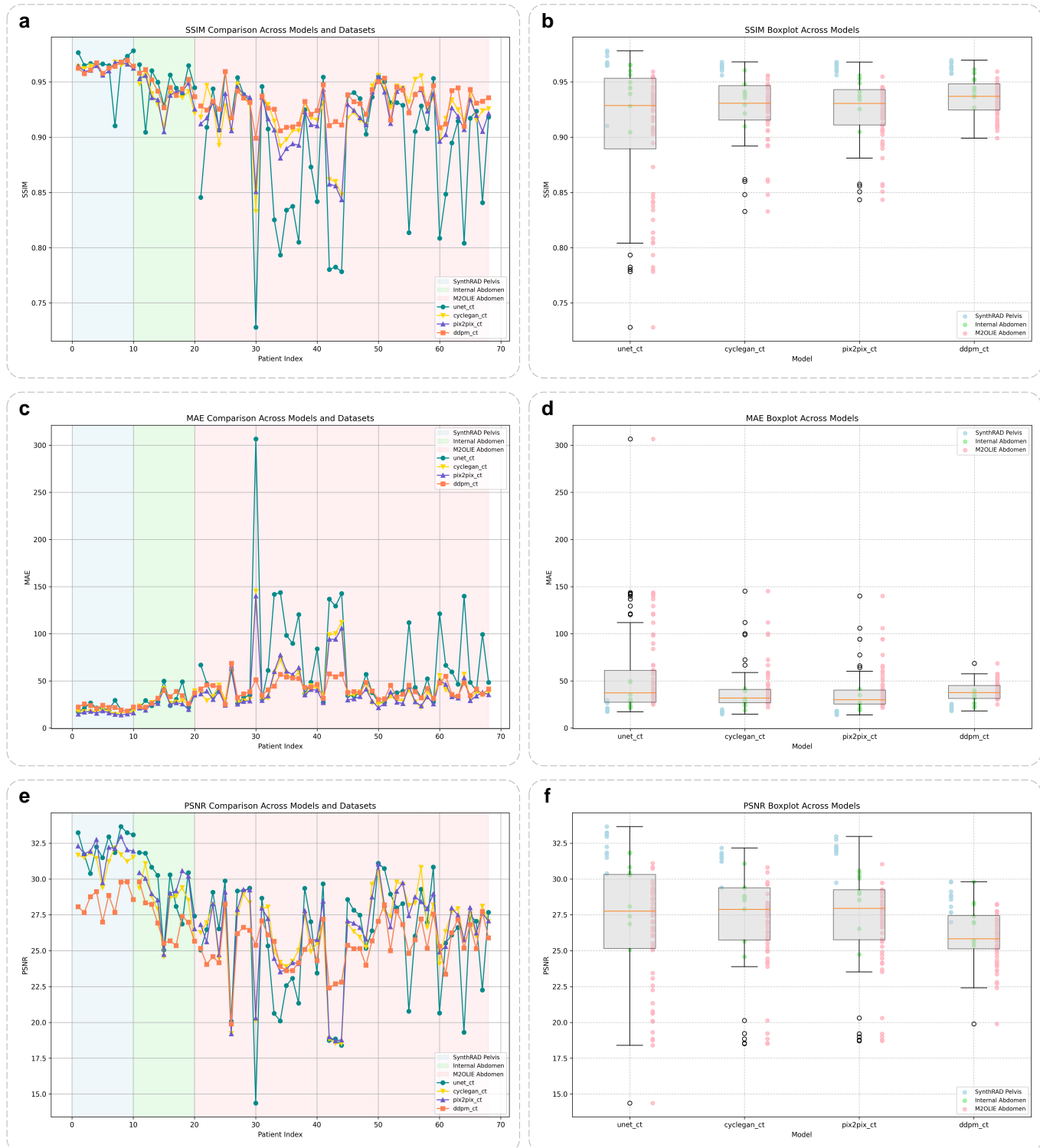


**Fig. 4.** Comparison of metric across models and datasets by line charts and box plots. This figure illustrates the performance of the four deep learning models—UNet, CycleGAN, pix2pix, and DDPM—on 68 test patients across three distinct datasets. The datasets are visually separated by the different background colors in line charts and the different point colors in box plots to facilitate comparative analysis, with blue standing for the SynthRAD Pelvis dataset, green standing for the Internal Abdomen dataset, and pink standing for the M2OLIE Abdomen dataset. Figures (a), (c), and (d) present line charts for SSIM, MAE, and PSNR, with the patient index on the x-axis. Figures (b), (d), and (f) display box plots for SSIM, MAE, and PSNR, with the x-axis representing the different models

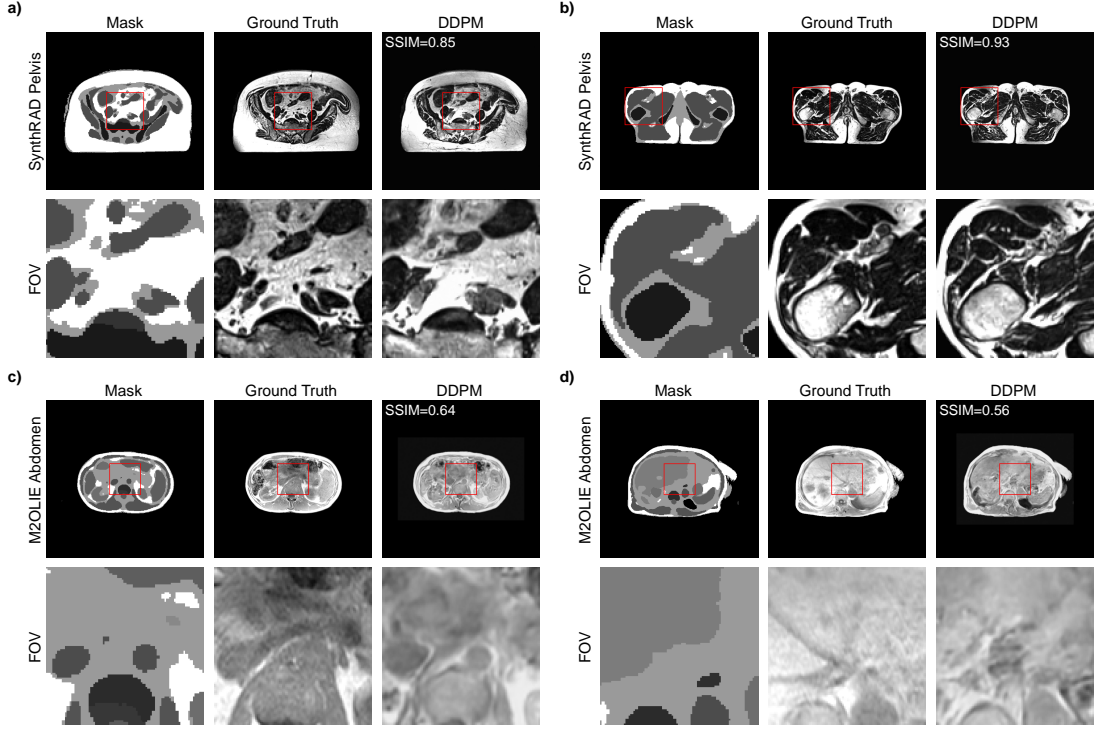


**Fig. 5.** Qualitative comparison of synthetic MR images generated by DDPM across two MR datasets. This figure presents representative slices of synthetic MR images for two datasets, showcasing the input masks (left column) and the corresponding outputs from the DDPM model (right column). Key quantitative metrics, including SSIM, PSNR, and MAE, are displayed to evaluate the model's performance. The rows highlight different anatomical structures, with red boxes marking fields of view (FOVs) for detailed comparison. Enlarged views of the FOVs are provided to illustrate structural and textural fidelity between the input masks and the generated MR images.

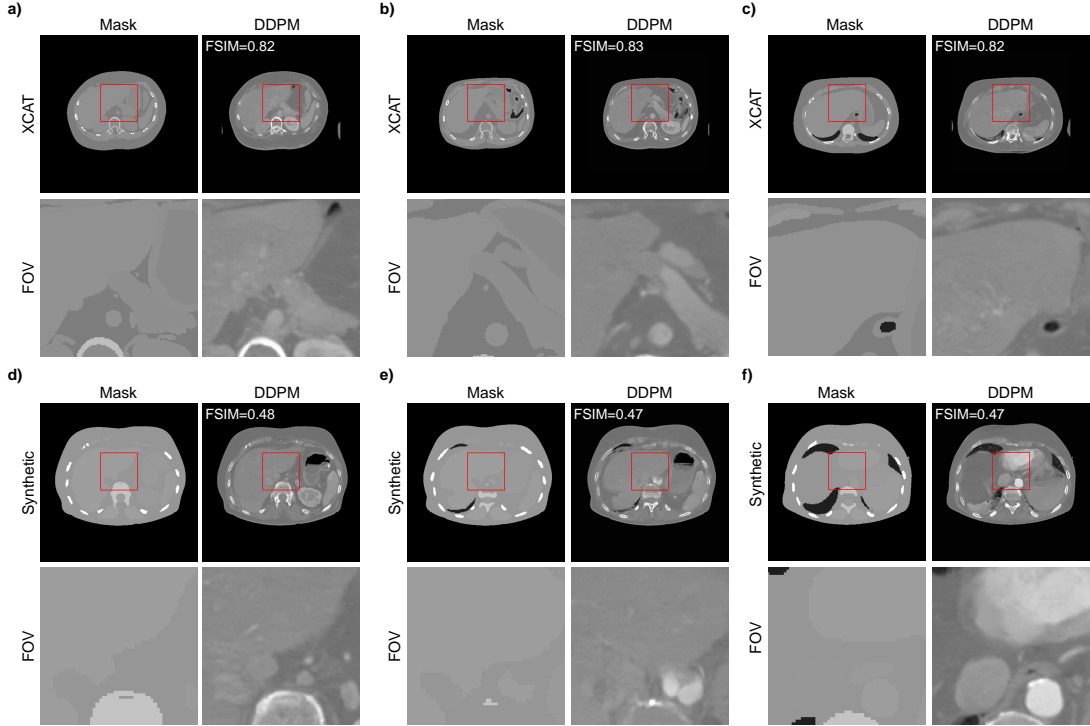


**Fig. 6.** Qualitative Assessment of Synthetic CT Images Generated by DDPM for XCAT and Synthetic Data. This figure presents representative slices of XCAT-masks and synthetic CT images, showcasing the input masks (left column) and the corresponding outputs generated by the DDPM model (right column). Feature Similarity Index (FSIM) is displayed for each example to evaluate the structural and intensity similarities between the generated images and the real CT images. Red boxes indicate fields of view (FOV), with magnified views provided below each slice to highlight fine details and differences in texture and intensity. This assessment emphasizes the model's performance on digital phantoms without ground truth.

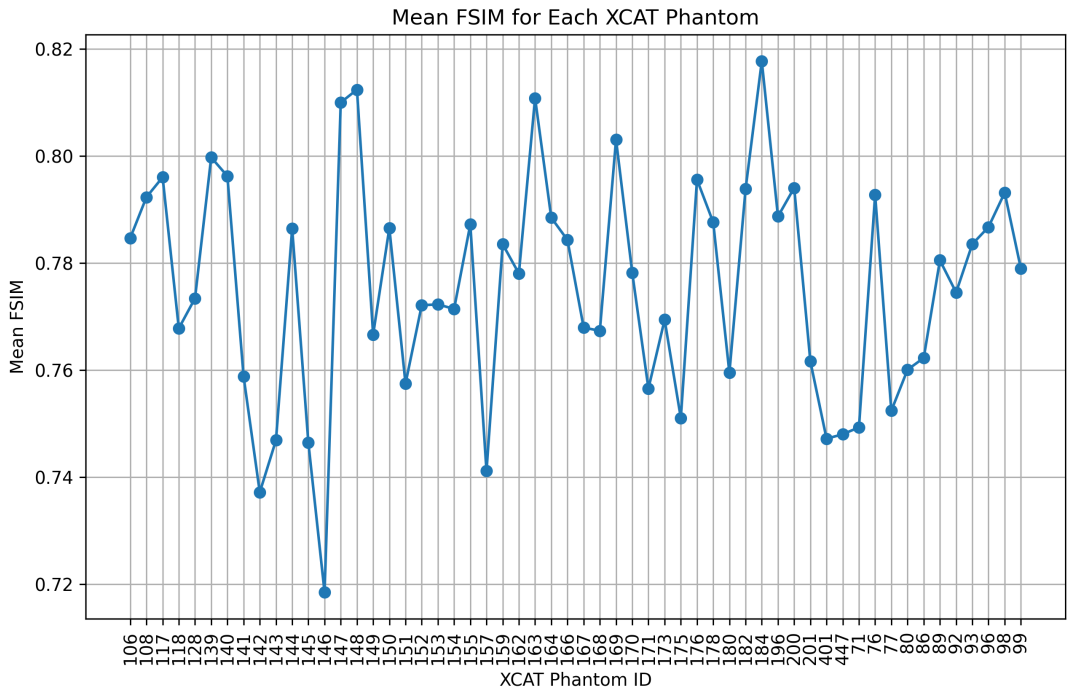


**Fig. 7.** Mean FSIM for Each XCAT Phantom. The figure presents the mean Feature Similarity Index Measure (FSIM) for synthetic images generated for each XCAT phantom. FSIM quantifies the perceptual similarity of the images by evaluating feature consistency, such as edges and textures. Most phantoms exhibit FSIM values exceeding 0.75, indicating high-quality synthetic image generation with well-preserved structural details. Variations in FSIM across phantoms may arise from differences in anatomical features and image complexity inherent to each phantom.

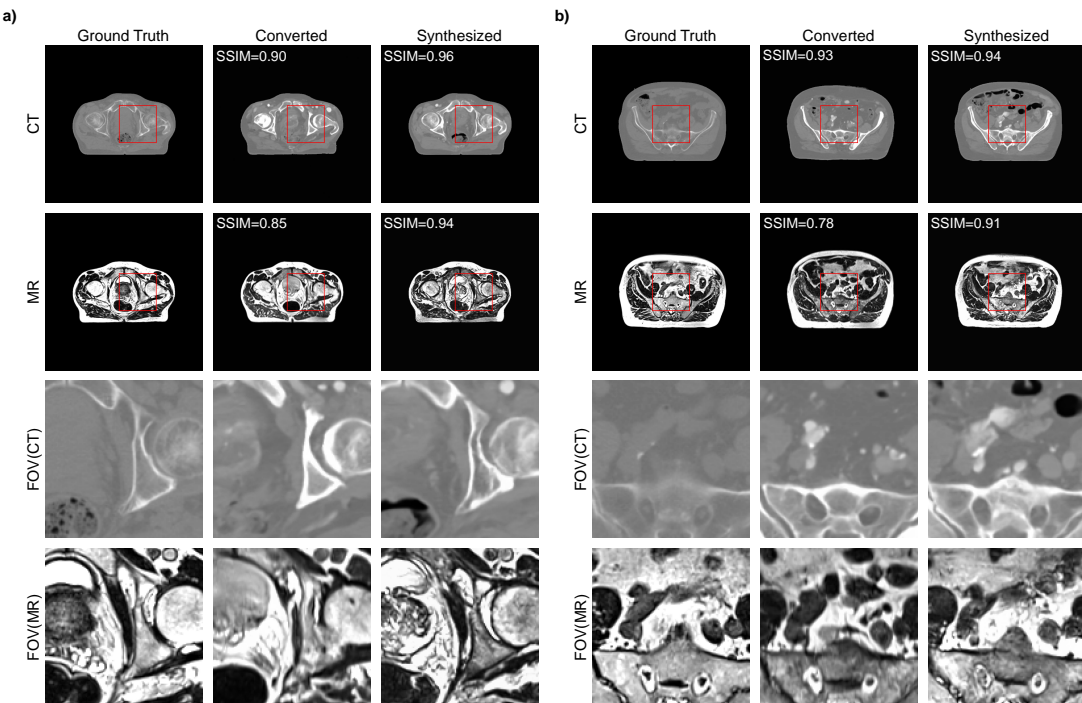


**Fig. 8.** Qualitative and Quantitative Comparison of Ground Truth, Converted, and Synthesized Images for CT and MR Modalities. This figure presents representative image slices from CT (top row) and MR (bottom row) modalities, comparing the ground truth images, converted images, and synthesized images from Experiment I and II. The converted images are generated using the masks from the opposite modality. Specifically, converted CT images are produced using masks from the MR modality, and vice versa. Each modality includes two sets of comparisons, highlighting Fields of Views (FOVs) marked by red boxes. Quantitative metrics, including SSIM, PSNR, and MAE, are provided for each example to evaluate structural fidelity, intensity consistency, and overall error. Enlarged views of the FOVs are shown below each row to emphasize fine structural and textural details, facilitating a detailed comparison between ground truth, converted, and synthesized outputs.

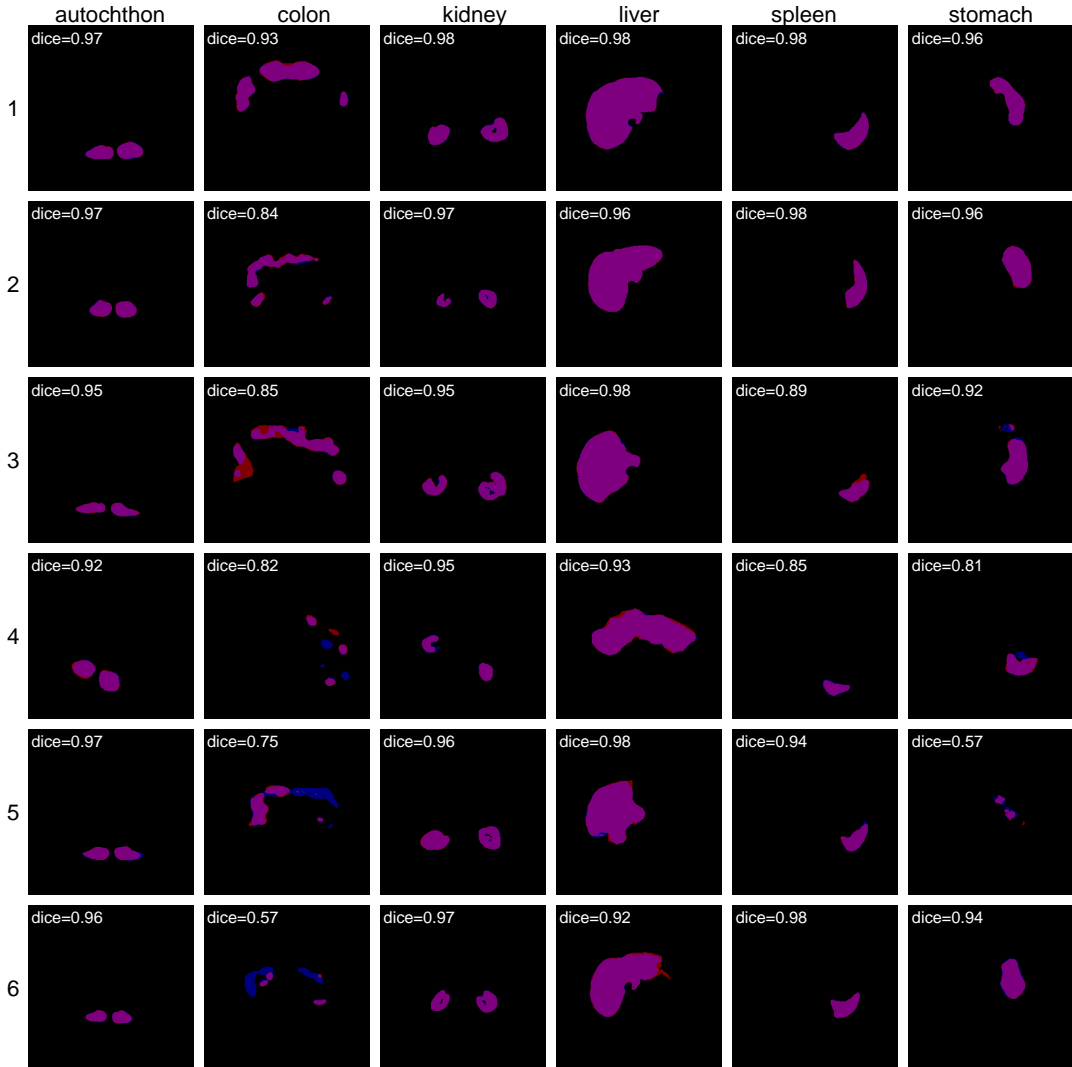


**Fig. 9.** Organ segmentation results with dice scores across different organs and cases. This figure displays the segmentation overlaps for six organs (autochthon, colon, kidney, liver, spleen, and stomach) across six cases. The red regions represent segmentations from the ground truth images. The blue region represent the segmentations from the synthetic images. The purple regions represent the overlap, while non-overlapping areas indicate segmentation discrepancies. The Dice similarity coefficient (Dice) is calculated for each organ and displayed above each panel. The results demonstrate the consistency between segmentations derived from synthetic CT images and those from ground truth images, with higher Dice scores indicating better agreement.

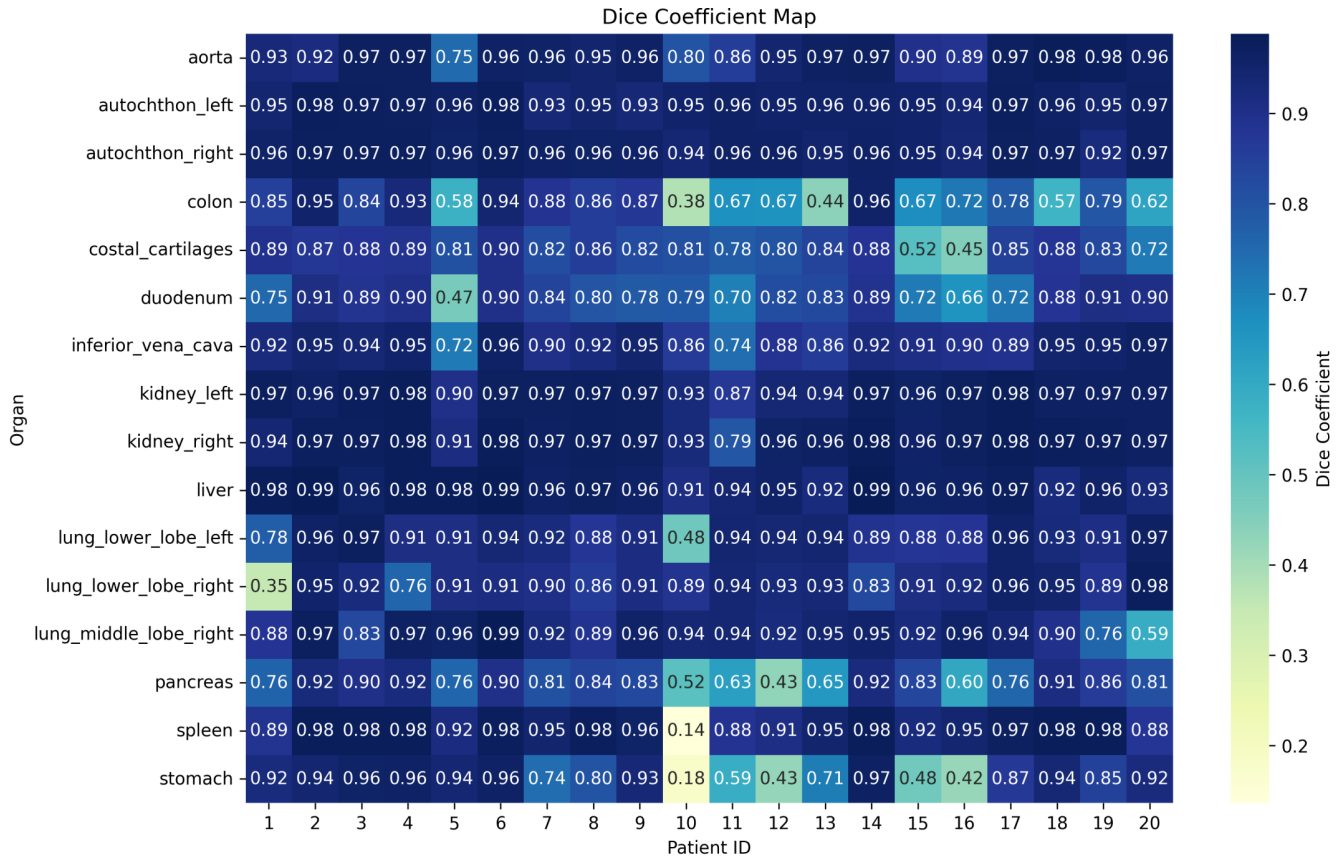


**Fig. 10.** Dice coefficient heatmap for organ segmentation across patients. This heatmap illustrates the Dice similarity coefficients for organ segmentation across 20 patients and 16 abdominal organs, from aorta to stomach. Each cell represents the Dice coefficient for a specific organ and patient, with higher values (darker blue) indicating better segmentation overlap between segmentations derived from synthetic CT images and those from ground truth images. The color gradient highlights performance variability, with lighter shades revealing lower segmentation accuracy. This visualization provides a comprehensive overview of the consistency between segmentations derived from synthetic CT images and those from ground truth images, identifying organs or cases with higher or lower agreement.